Summer 8-24-2022

Parametric Design of a Manifold for a Hollow Micropillar Evaporator for use in High Heat Flux Applications

Alex Dutton

Washington University in St. Louis

Recommended Citation

Dutton, Alex, "Parametric Design of a Manifold for a Hollow Micropillar Evaporator for use in High Heat Flux Applications" (2022). *McKelvey School of Engineering Theses & Dissertations*. 759.
https://openscholarship.wustl.edu/eng_etds/759

WASHINGTON UNIVERSITY IN ST. LOUIS

McKelvey School of Engineering

Department of Mechanical Engineering and Materials Science

Thesis Examination Committee:
Damena Agonafer, Chair
Dave Peters
Jackson Potter

Parametric Design of a Manifold for a Hollow Micropillar Evaporator for use in High Heat Flux Applications

by

Alexander Dutton

A thesis presented to
the McKelvey School of Engineering
of Washington University in
partial fulfillment of the
requirements for the degree
of Master of Science

August 2022
St. Louis, Missouri

Table of Contents

List of Figures

Acknowledgments

I would like to thank Damena Agonafer, Vivek Manepelli, Kidus Guye, and the rest of the students in the NEIT Lab for their support and technical insight into this work. I would also like to thank Mark Specter and the Office of Naval Research for providing funding for this project under the SBIR grant 'Advanced Thermal Management of Power Converters' (N21A-T012-0110). I would also like to thank Michael Ellis and Advanced Cooling Technologies for providing access to their testing facilities, supplies, and resources used in the testing of my initial prototypes.

Additionally, I would like to thank my friend Alex Levy, without whose advice, encouragment, and feedback this would not have been possible.

Lastly, I would like to thank my mom and dad. Thank you for believing in me and supporting me along this rollercoaster. This work is just as much yours as it is mine.

Alexander Dutton

Washington University in St. Louis
August 2022

ABSTRACT OF THE THESIS

Parametric Design of a Manifold for a Hollow Micropillar Evaporator for use in High Heat Flux Applications

by

Alexander Dutton

Master of Science in Mechanical Engineering

Washington University in St. Louis, 2022

Professor Damena Agonafer, Chair

With the failure of Dennard Scaling and changes in electronics packaging leading toward 2.5 and 3D packages, the current methods of thermal management are failing to keep up with rising heat fluxes. In order to manage these rising heat fluxes, engineers and scientists are looking towards two phase cooling and microchannel flows.

Many forms of novel thermal management are currently being investigated as means to address the thermal challenges present in modern microelectronics, including flow boiling, pool boiling, and direct liquid cooling. One technology of interest is evaporative cooling using continuously fed micro-droplets. High evaporation rates can be achieved by using engineered hollow micropillar structures, and these devices have been shown to reject upwards of 280 watts/cm^2 with water as a working fluid. Current systems only address the management of high heat fluxes, and do not consider the packaging, liquid delivery mechanisms, and thermal resistance constraints that are present in actual electronic systems.

This paper seeks to develop a manifold and enclosure to allow a hollow micropillar evaporator to be implemented on a physical device. Geometric, thermal, and hydraulic constraints are created to define the geometry of a manifold to deliver liquid to the evaporator. The main challenge present in the design of the manifold and enclosure is to ensure uniform delivery of the working fluid to each pillar in the array while minimizing the thermal resistance between the bottom of the manifold and the evaporator.

Two different layouts are presented to achieve this balance between uniform flow rate and minimal thermal resistance. The first architecture flows the working fluid laterally underneath the evaporator, and the second incorporates a 180 degree turn of the working fluid to flow vertically before reaching the evaporator. 2D parametric CAD models are created of both layouts to simulate a range of design variables. First, an analytical resistance model is developed to analyse the lateral flow geometry. Then a computational fluid dynamics (CFD) model is created and used to run a multi-factor design of experiments (DOE) which allows for the comparison of several geometric variables along with different viscosities, densities, and fluid velocities on the flow rate through each pillar in the system. Since there is not a specific device or implementation currently in mind, this work seeks to develop an understanding of the fundamental physics present in the single phase fluid flow leading to the evaporator. Interactions and main effects are identified from the DOE, with only the height of the liquid channel dictating the performance of the system. The fluid density, viscosity, and flowrate does not significantly impact the distribution of liquid through each pillar at the values under study.

Lastly, a physical prototype is developed for use with R245-fa refrigerant. The final prototype incorporates a 3D manifold, liquid overflow channels, and mating features to aid in the assembly of the evaporator, copper heat spreader, and manifold. Material properties are assessed to ensure compatibility with R245-fa, along with feature size requirements. Several prototypes are assembled and are tested to seal up to 15 bar. A loop thermosyphon utilizing the evaporator was developed and shown to evaporate the refrigerant and create a two phase cycle, however full data was not able to be collected on the experiment.

The developments presented in this thesis provides the foundation for future implementation of hollow micropillar evaporators. Additional work can be done using the DOE to create a reduced order model (ROM), which would allow for rapid evaluation of future potential geometries, flow rate, and working fluids. Manufacturing limits and materials are suggested which allows for faster development of physical prototypes. Future work on the upper manifold, specifically the bifurcation from one inlet to a square outlet needs to be addressed. Lastly, a multi-phase numerical model needs to be developed to understand the change in evaporation rate as the droplets grow or shrink, as well as transient effects that might arise due to startup or variation in thermal loading.

Chapter 1

Introduction and Motivation

1.1 Introduction

The increase in heat fluxes within microelectronics devices over the last few decades has driven various advancements in thermal management. Single phase cooling is an area of active research, where developments in manifolds are currently under study. Piazza et al. studied the scaling of embedded microchannel with 3D manifold heat sinks (EMMC's) from 5x5mm^2 up to 20x20 mm^2, and demonstrated that as EMMC's scale, the temperature gradient along the cold plate increases as well as the required pumping power [14].

Two phase systems are investigated as a means to address the high heat fluxes without the necessary high pumping power required by single phase cooling. Evaporative cooling has been investigated by Wang et al. using micro-channels to create concave droplets, and has rejected heat fluxes up to $6KW/cm^2$. The concave droplets were also shown to have similar performance between uniform and nonuniform heat fluxes. This demonstrates that evaporative cooling has the robust potential to address current needs in microelectronics. However, concave droplets suffer from several draw backs. The negative contact angle and corresponding negative Laplace pressure can lead to the onset of premature boiling. Additionally, concave droplets have lower evaporation rates due to their low surface area to volume ratio.

The Nanoscale Energy and Interficial Transport Lab at Washington University in St. Louis has been investigating the implementation of convex micro droplets as a method to mitigate the drawbacks of concave droplets. Initial numerical investigations on the evaporation rates of single droplets pinned atop hollow micropillars have been conducted and shown up to a 42% increase in the evaporation rate when compared to sessile droplets on flat surfaces [4]. Additionally, the impact of micropillar shape on the contact line dynamics has also been studied, and the droplet growth behavior has been characterized on several different pillar shapes [10].

1.2 Current Prototypes

These initial successes and characterization of the contact line dynamics of convex micro-droplets has lead to the creation of a prototype evaporator and test manifold to experimentally study their behavior. 1x1mm^2 and 5x5mm^2 arrays of micro pillars were manufactured using silicon micro-fabrication techniques. The 5x5mm^2 evaporator is shown below in fig. 1.1 and 1.2.

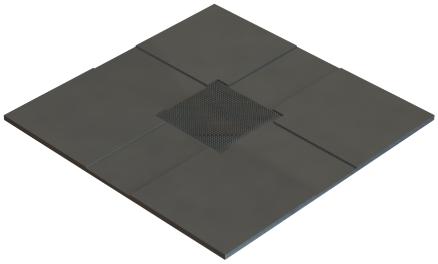

Figure 1.1: Render of an Isometric view of the hollow micropillar evaporator

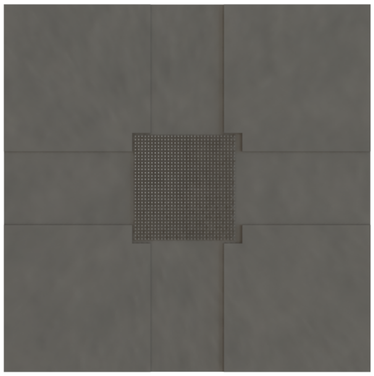

Figure 1.2: Render of the top of the Evaporator

The prototype manifold is shown in fig. 1.3 and 1.4 below.

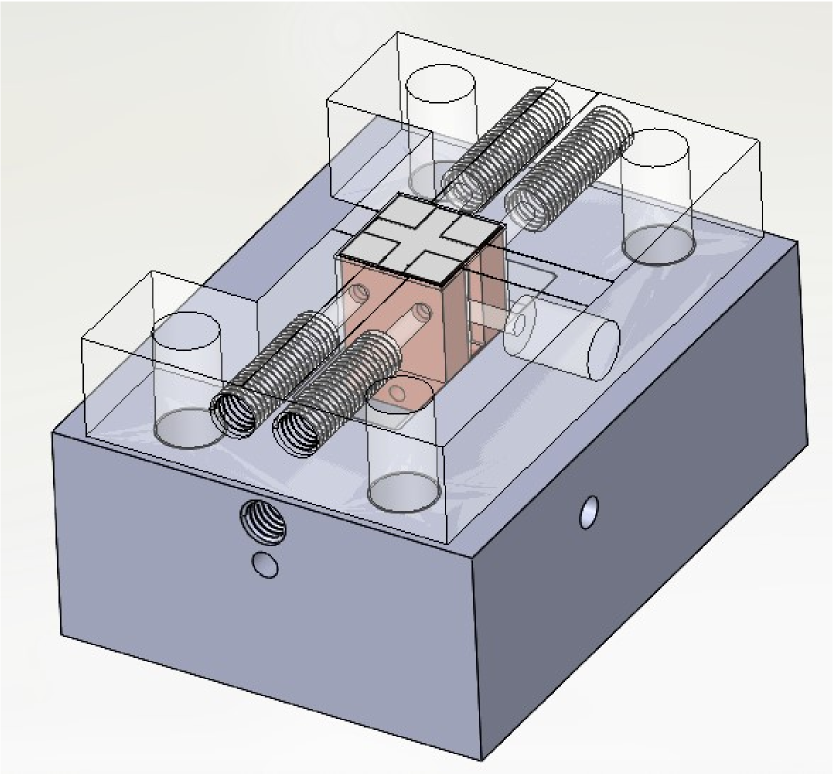

Figure 1.3: Isometric view of the experimental manifold

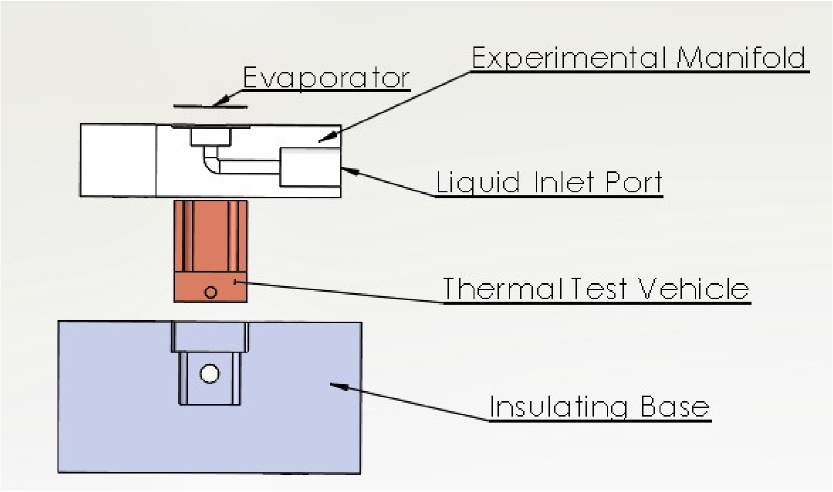

Figure 1.4: Exploded/Section View of the Experimental Manifold

Since the main effort of these manifolds is to test the performance of micropillar array, a large reservoir is placed underneath the array, and the working fluid flows under the evaporator and develops in the reservoir before flowing up through the array. The reservoir acts as a buffer between the inlet port and the evaporator, as the flow is given enough space to dampen out any non uniformities introduced by the change in flow direction. This ensures that the pressure at the entrance to the evaporator is uniform, which allows for uniform flow through each micropillar. The use of the reservoir for feasibility testing allowed for rapid development of the prototype manifold, however it neglects some of the design requirements for use in a physical device

This can clearly be shown in fig. 1.4, as the liquid inlet is placed below the evaporator, and the manifold makes a turn upwards before reaching the reservoir.

1.3 Manifold Design Goals

1.3.1 Equal Flowrate through each Pillar

The difficulty of pumped two phase systems comes from the need to match the evaporation rate with the flowrate supplied by the pump. Passive two phase systems remove this constraint, as the flowrate through the system is driven by the heat load, such as in thermosyphons or heat pipes [17]. These systems are not able to support large heat fluxes since they are often limited by geometry because the pressure head in the system is often driven by gravity. To address these geometric issues, engineers look to pumped two phase systems in order to achieve higher heat fluxes.

As shown in the current experiments on the micropillar arrays, the uniform delivery of the working fluid is critical to the performance of the evaporator. In order for optimal performance of the evaporator, the flowrate supplied to the evaporator and the evaporator must be matched, or else flooring or dry out will ensue. This constraint is compounded by the need to ensure this flowrate balance through every droplet in the array on the manifold.

Droplet Contact Line Dynamics and Evaporation Rate

Before designing the manifold to deliver liquid to the evaporator, it is critical to understand the different factors that influence the evaporation rate from each droplet in the array. When considering working fluids for a two phase system, the two main options are water, due to its high latent heat of vaporization, and dielectric fluids, as they are able to come into direct contact with silicon devices. These two liquids behave very differently, with dielectric fluids having a very low surface tension, and therefor low contact angles, while water has a much higher surface tension. The main factors that drive the evaporation rate for low contact angles, and for hemispherical droplets are shown below, where eqn. 1.1 and 1.2 determine the flow rates for low contact angle and hemispherical droplets respectively.

$$J(r) = \frac{2}{\pi}\frac{D(n_s - n_\infty)}{\sqrt{R_i^2 - r^2}} \tag{1.1}$$

$$J(r) = \frac{D(n_s - n_\infty)}{R_i^2} \tag{1.2}$$

J(r) is the evaporation rate [kg/s], D is the diffusion constant $[\frac{m^2}{s}]$, n_∞ is the ambient vapor density $[\frac{kg}{m^3}]$, n_s is the saturated vapor density$[\frac{kg}{m^3}]$, R_i is the radius of the droplet [m], and r is the variable distance from the center of the droplet [m] [15]. From these two equations, it is clear that the evaporation rate J(r) can be maximized by minimizing the size of the droplet.

Large pressure heads are required to form stable concave droplets atop a micropillar, when compared to convex droplets, as shown in fig. 1.5. The required height of a water column to achieve the pressure heads to for them convex droplets shown in fig. 1.5 is 4.1m, which is impractical for many microelectronic cooling applications.

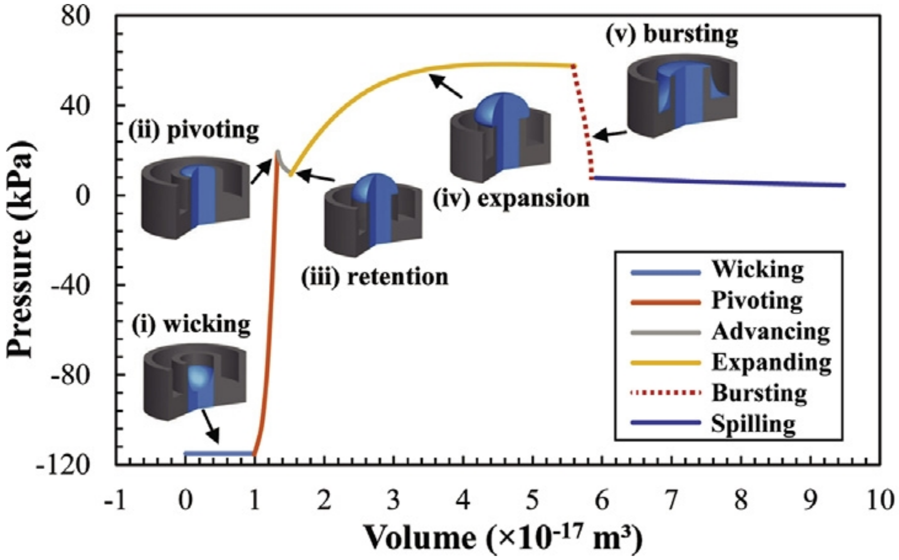

Figure 1.5: Plot of the Pressure vs Water Droplet Volume Through Its Growth Atop a Micropillar [4]

Both eqn. 1.1 and 1.2 demonstrate that the evaporation rate is inversely proportional to the droplet radius. Therefore, for any droplet, the desired point along the curve shown in fig. 1.5 would be right at the point of retention. As the droplet expands, the evaporation rate will decrease. This demonstrates that the pressure difference between the liquid and vapor phase must be tightly controlled for optimal evaporation rates.

1.3.2 Minimizing Thermal Resistances

When designing thermal management systems, a common method of analyzing thermal performance is the thermal resistance of the system. For this system, the thermal resistance can be considered to be the conduction resistance between the heat generating element, and the evaporator. An example geometry for the conduction path from the heat generating element to the evaporator is shown below, where heat is conducted from the copper micro-posts up into the evaporator.

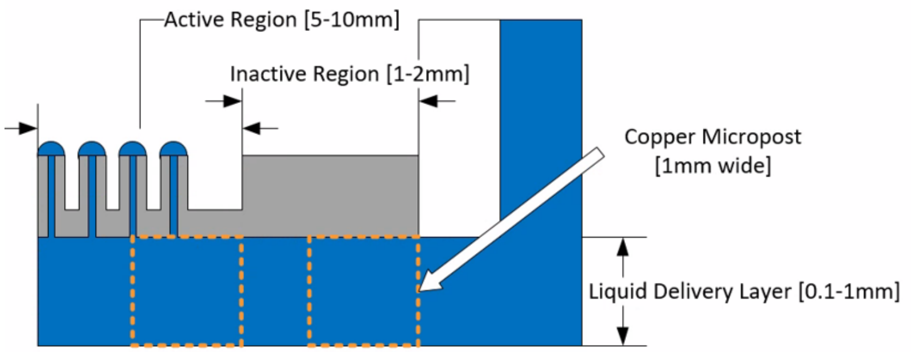

Figure 1.6: Example Geometry That Includes the Use of Copper Microposts

The design of the shape and array of the micro-posts is outside the scope of the initial manifold development, so the copper posts are assumed to be 1x1mm^2. The conduction resistance through each of the posts can be given by eqn. 1.3 [6].

$$R_{post} = \frac{L}{k * A} \tag{1.3}$$

L is the height of the copper posts [m], or the Liquid Delivery Layer (LDL) height shown in fig. 1.6, k is the thermal conductivity of the copper $[\frac{W}{m*^{\circ}K}]$, A is the area of a single post$[m^2]$, and R_{post} is the thermal resistance $[\frac{^{\circ}K}{W}]$. Since there are multiple copper posts, the total resistance of the system can be calculated from the resistance network shown below in fig. 1.7.

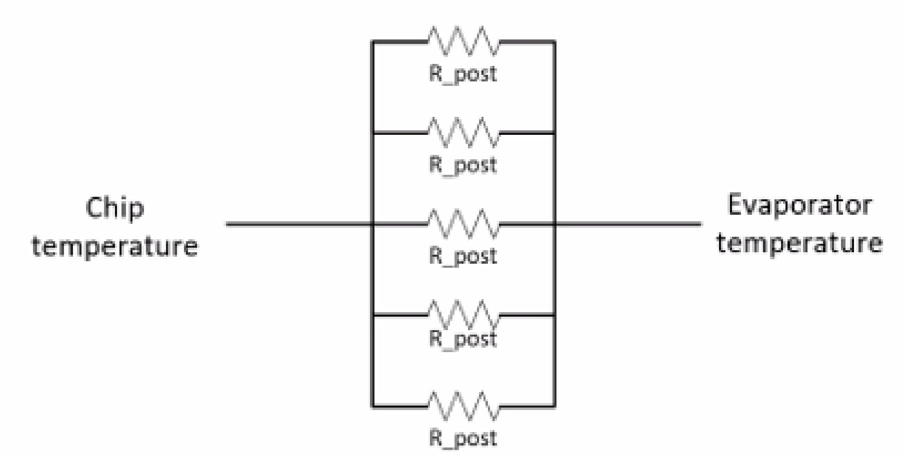

Figure 1.7: Thermal Resistance Network for the Evaporator

Where the total resistance can be calculated from eqn. 1.4.

$$R_{total} = (\sum \frac{1}{R_p})^{-1} \tag{1.4}$$

In order to make the system more responsive to sudden changes in heat loads, as well as to decrease the difference in temperature between the heat source and the evaporator, the thermal resistance must be minimized. From eqn. 1.3 and 1.4, the thermal resistance of the manifold can be minimized by minimizing the distance between the evaporator and the heating element. This height will be referred to as the Liquid Delivery Layer height, or LDL height.

1.3.3 Geometric Constraints

In order to successfully implement the hollow micropillar evaporator onto a chip, there are several geometric and packaging constraints that must be placed on the delivery of the working fluid:

1. The inlet to the manifold cannot be placed below the evaporator, as that is where the heat generating element is
2. There must be sufficient inactive area to bond the silicon evaporator to the manifold

1.3.4 Constraint Summary

A list of all of the constraints used to design the manifold is shown below.

1. The pressure under each micropillar should be the same in order to ensure the same sized droplet, and therefore the same evaporation rate from each droplet
2. The LDL height must be minimized
3. The inlet to the manifold cannot be placed below the evaporator, as that is where the heat generating element is
4. There must be sufficient inactive area to bond the silicon evaporator to the manifold

Chapter 2

Design Exploration

Several assumptions are made in order to simplify future design work. First, this work assumes that the flow up to the droplet is not impacted by the droplet shape, and the delivery of liquid up to the droplets can be simulated with single phase flow. This assumption comes from the clear delineation between the liquid and vapor phases. Additionally, since the dominant mode of heat transfer is evaporation, the convection from the heat source into the bulk fluid is not considered. When taking into account these assumptions, the only boundary conditions on the following analysis are a constant mass flow through the system, and the saturation pressure of the droplet at the outlet. The following design work details the generation and study of several parametric geometries that can be analysed using the two boundary conditions developed here.

2.1 Geometries Under Study

2.1.1 Lateral Flow

The two driving constraints on the design of the evaporator are to minimize the thermal resistance, and to introduce the liquid from the sides of the evaporator. The simplest design would be to flow the liquid horizontally between the evaporator and the heat generating element. This can be analyzed as flow between parallel plates where one of the walls is porous. The geometry would eliminate the need for additional geometric features to turn the direction of the fluid flow and would allow for a minimal thermal resistance by reducing the distance between the evaporator and the heat generating element. An example geometry of a device with a Lateral Flow configuration is shown below in fig. 2.1.

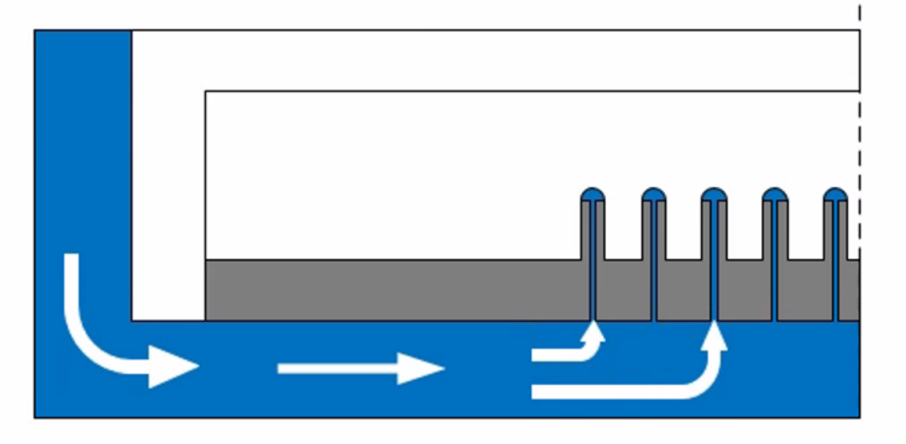

Figure 2.1: Diagram of Lateral Flow Architecture

2.1.2 180° Turn

In order to mitigate the issues of a lateral pressure drop that is present in the Lateral Flow geometry, the 180° Turn geometry is introduced. The wall of the manifold is extended down into flow path, as shown in fig. 2.2. This forces the liquid to begin to turn and flow upwards before reaching the active area of the evaporator.

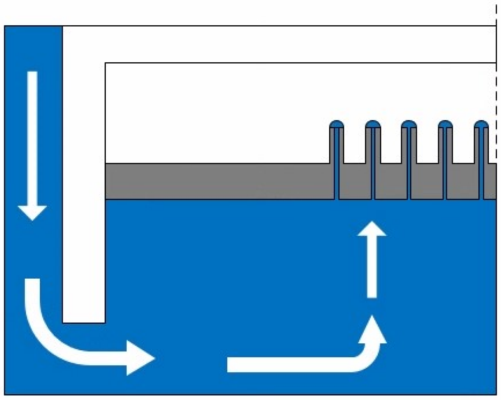

Figure 2.2: 180° Turn Diagram

2.2 Analytic Models

An analytical model of the Lateral Flow Geometry is created using a resistor network analogy. Figure 2.3 below shows the resistor network approximation for the Lateral Flow Architecture

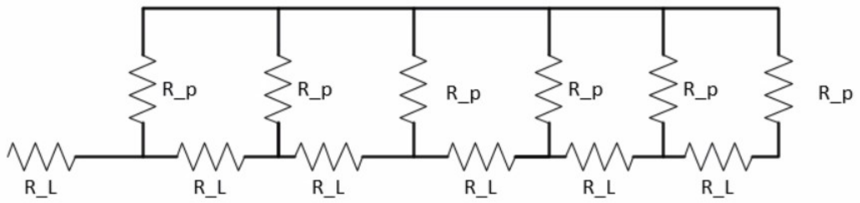

Figure 2.3: Resistor Network for Lateral Flow Architecture

R_L and R_p are the hydraulic resistance of the flow underneath the evaporator and the resistance to flow through each micropillar, respectively. First, a 2D resistance approximation is created. This treats both the flow under the evaporator and the flow through each micropillar as flow between parallel channels. All flowrates and resistances are therefor per unit depth, or $\frac{m^3}{s*m}$ and $\frac{kg}{s*m^4*m}$ for this formulation. This allows for a comparison between the analytical model and 2D CFD. The equations below are the resistances for both the flow under the evaporator and the flow through each pillar.

2.2.1 2D resistance formulation

The hydraulic resistances for the 2D formulation of the resistor network are shown in eq. 2.1 and 2.2

$$R_l = \frac{6 * \mu * pillar_{spacing}}{4 * Height^3} \tag{2.1}$$

$$R_p = \frac{6 * \mu * pillar_{length}}{4 * pillar^3_{diameter}} \tag{2.2}$$

μ is the dynamic viscosity $[\frac{kg}{m*s}]$, and the pillar spacing, length, diameter, and Height are all in [m]. After validating this formulation against 2D CFD, the resistance model is expanded into 3 dimensions in order to more accurately model the impedances present in the micropillars. Add in the variable names

2.2.2 3D Resistance formulation

In the 3D formulation, the flow under the evaporator is treated as flow between parallel plates with a known depth where the flow resistance is shown in eqn. 2.4. The flow through the micropillars is modeled as Haagen Pousalle Flow, and the resistance is calculated with eqn. 2.3.

$$R_p = 128\mu * pillar_{length}/(\pi * pillar^4_{diameter}) \tag{2.3}$$

$$R_l = 6\mu S/(4H^3W) \tag{2.4}$$

S is the spacing between each pillar [m], H is the height of the channel underneath the evaporator[m], and W is the width of the fluid channel [m] [12]. This 3D formulation allows for a more accurate prediction of the impedances present in the system, as the diameter of the micropillars is an order of magnitude smaller than the height of the liquid delivery layer.

2.2.3 Solving The Resistor Network

The individual flowrates through each pillar can now be solved for after determining the individual resistance in the system. This resistor network is analogous to a resistor ladder that is commonly used in electronic circuits, and can be solved using Kirchhoff's Current Law at each node in the system. A system of equations can be created using the flowrate balance at each node. An example is shown in eq. 2.5. Figure 2.4 is provided for reference.

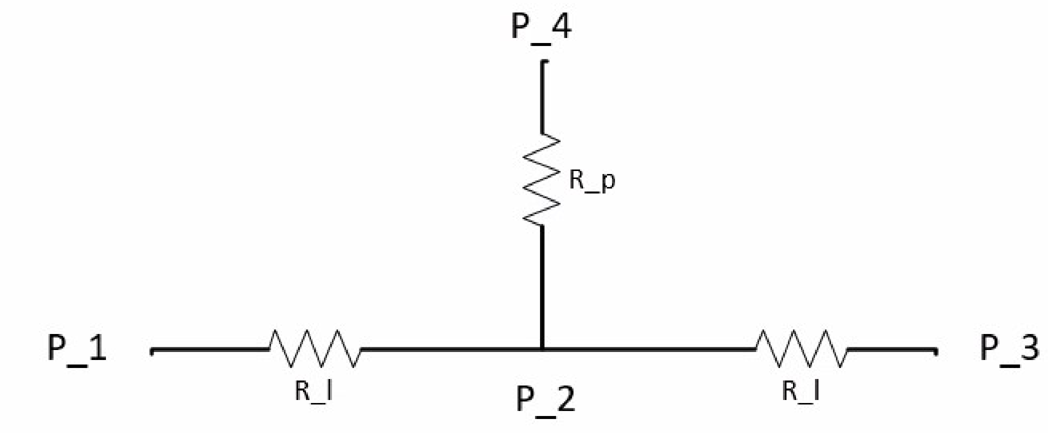

Figure 2.4: Sample Resistor Network

$$\frac{P_2 - P_1}{R_l} + \frac{P_2 - P_3}{R_l} + \frac{P_2 - P_4}{R_p} = 0 \tag{2.5}$$

Where P_{1-4} are the pressures at each node [Pa], and R_l and R_p are the hydraulic resistances of the micropillar and liquid delivery layer, respectively. Since only the pressure delta over the entire domain is of interest, P_4 is set to 0 to simplify the calculations. A Matlab script was written to iterativley loop through each node in the resistor network to form a system of equations for the entire network. In order to solve the system in fig. 2.4 it is assumed that the outlet pressure of every micropillar is the same. If the size of the droplets changes across the array, the system resistance begin to change and is then coupled to the flowrate through each pillar. In order to simplify the initial design exploration of the geometries for the micropillar evaporator, it is assumed that each pillar is the same size to avoid this coupling.

2.3 Parametric Design Study

The main benefit of the 180 turn geometry is that the nature of the flow is inherently 2D, as the flow is allowed to move laterally and vertically. CFD is used to analyze this geometry, since it cannot be simplified into a network of pipes or other analytical model.

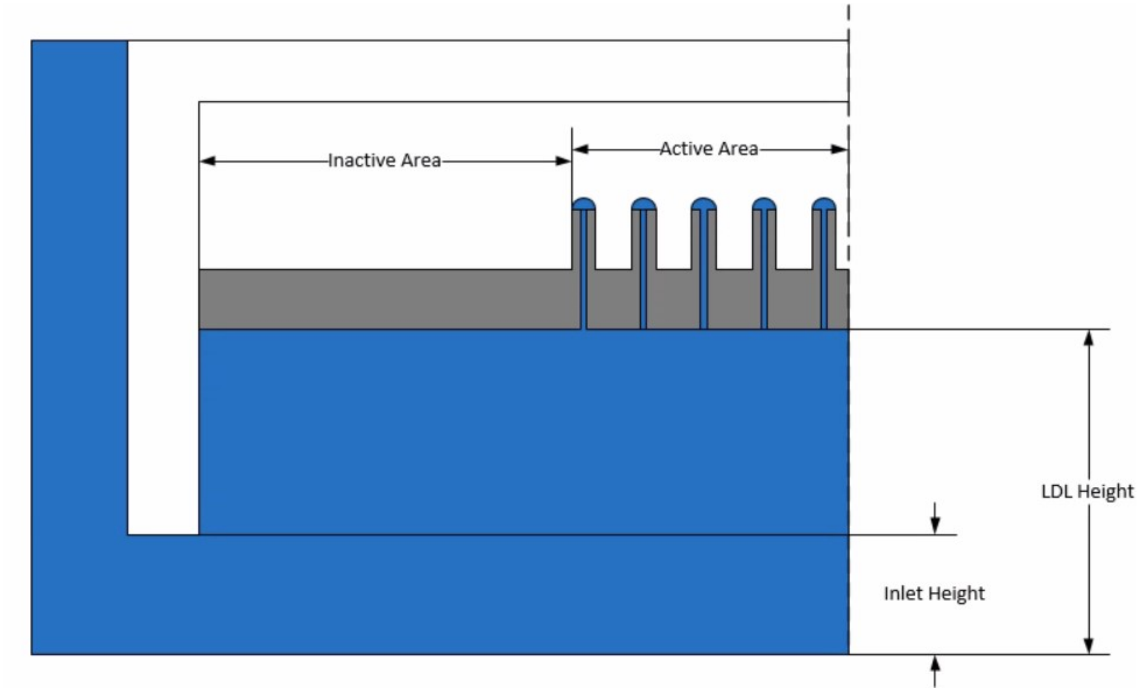

Figure 2.5: 180° Turn Design parameters Diagram

The active area is the portion of the evaporator that contains micropillars, and the inactive is the portion that does not. The inactive area plays a role in both the delivery of the liquid to the active area, as well as serves as a mating and adhesive surface to attach the manifold to the evaporator. The LDL height is the distance the evaporator lies from the chip, and the Inlet Height is the distance the wall of the manifold lies from the chip. The Inlet height and the LDL height are the key differentiating features of the 180° turn platform from the Lateral Flow Platform, as they create a space for the liquid to turn and begin to flow upwards.

In addition to the four geometric parameters, three additional parameters are used to complete the design space: inlet flowrate, density, and viscosity of the working fluid. These three additional parameters will allow for future changes to the working fluid or target heat flux to be considered in the design of the manifold and liquid delivery system.

Below is a table of all of the values of each parameter that will be under study.

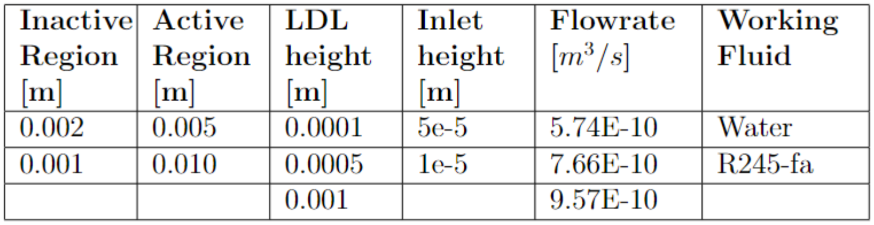

Inactive Region [m]	**Active Region [m]**	**LDL height [m]**	**Inlet height [m]**	**Flowrate** $[m^3/s]$	**Working Fluid**
0.002	0.005	0.0001	5e-5	5.74E-10	Water
0.001	0.010	0.0005	1e-5	7.66E-10	R245-fa
		0.001		9.57E-10	

Figure 2.6: Table of Design Parameters

2.4 Numerical Analysis

In order to get a better understanding of both of the geometries under study, a series of CFD simulations are conducted. The governing equations for steady, incompressible, laminar flow without gravity are shown below [2].

$$\nabla \cdot (\rho v) = 0 \tag{2.6}$$

$$\nabla \cdot (\rho v v) = -\nabla p + \mu \nabla^2 (v) \tag{2.7}$$

where eqn. 2.6 and eqn. 2.7 are the continuity and momentum equations, respectively. ρ is the density, v is the fluid velocity vector, and μ is the fluid viscosity $[\frac{kg}{m*s}]$. A commercial finite volume solver, Ansys Fluent 2021 R1, is used to discretize and solve the Navier Stokes equations. A coupled pressure-velocity algorithm is used to simultaneously solve a modified form of continuity as well as the momentum equations. Second order schemes are used to discretize both the pressure and momentum derivatives.

2.4.1 Geometry and Boundary Conditions

The computational domain for the CFD simulations is shown below in fig. 2.7

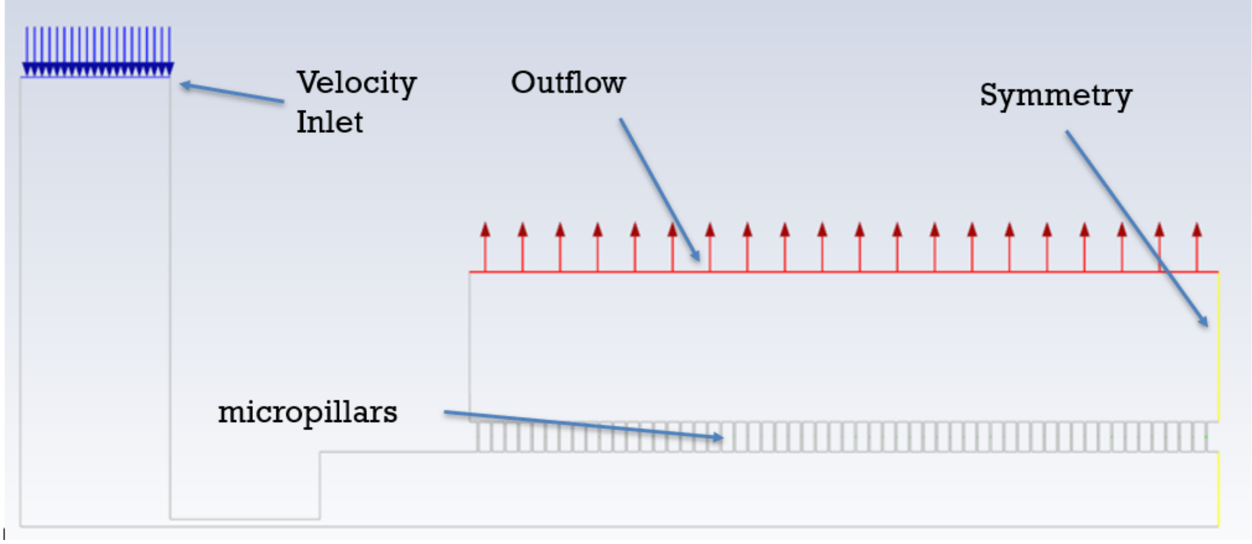

Figure 2.7: Image of the Computational Domain

The inlet velocity was calculated from previous experimental data, where a flowrate/pillar was calculated to be $4.531e{-}12\frac{m^3}{s}/pillar$. The number of pillars is determined parametrically by the equation below

$$Num_{pillars} = floor(W_{active}/2/S) \tag{2.8}$$

Where W_{active} is the active width of the evaporator [m], and S is the spacing between each micropillar [m], and floor rounds down the value to the nearest integer. The inlet velocity can then be calculated from the number of pillars, the flow rate per pillar, and the inlet width. This allows for the parametric model to change the inlet velocity according to the active area.

Symmetry is also used in this set of simulations to simplify the computational domain. The outlet boundary is specified as an outflow condition and the rest of the boundaries in the system are considered to be smooth walls. The outlet of the domain is adjusted to improve the convergence of the numerical simulations and is not used to study the flow of liquid after the outlet of the micro-droplets. These boundary conditions are used in the CFD for both the lateral and 180° turn geometries.

2.4.2 Initial Grid Independence Study

In order to shorten the computation time, it is not feasible to conduct a grid independence study for every point in the design space. Therefore, a grid independence study was conducted on one set of design points, and the same mesh parameters are used for the rest of the DOE. Below is a graph of the outlet static pressure vs the number of cells used in each solution.

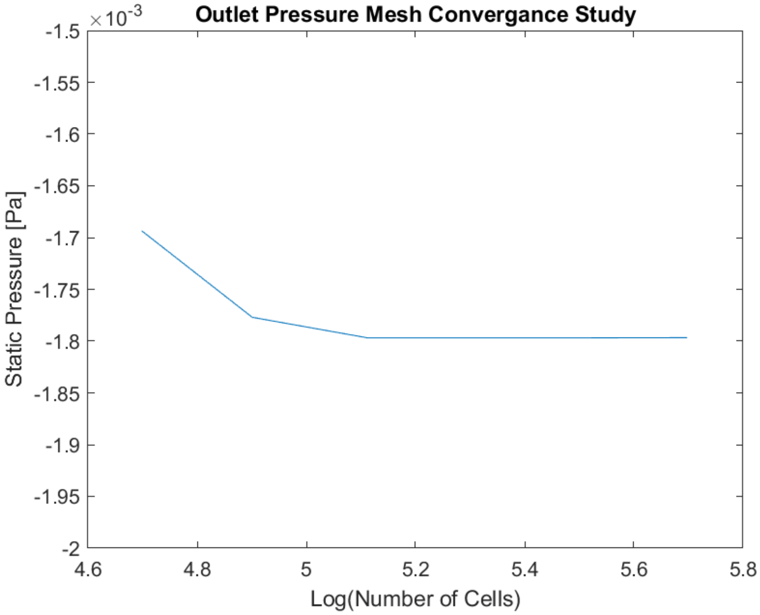

Figure 2.8: Grid Independence Plot of Outlet Static Pressure vs Number of Cells

This graph demonstrates that the solution is globally converged, as the outlet pressure reaches an asymptotic solution when mesh contains 130,000 cells. Since each simulation was conducted with the finest mesh of around 500,000 cells the solution can be considered grid independent. Additionally, all design points are considered converged when the residuals are below 1e-7.

2.5 Results and Analysis

2.5.1 Lateral Flow

Comparison with 1D approximation

First, the 1D resistance model is compared to the CFD results for the same geometry. This is used to validate the assumptions made in the resistance model. Figure 2.9 below shows the pressure in the Liquid Delivery Layer for the 1D resistor network and the 2D CFD.

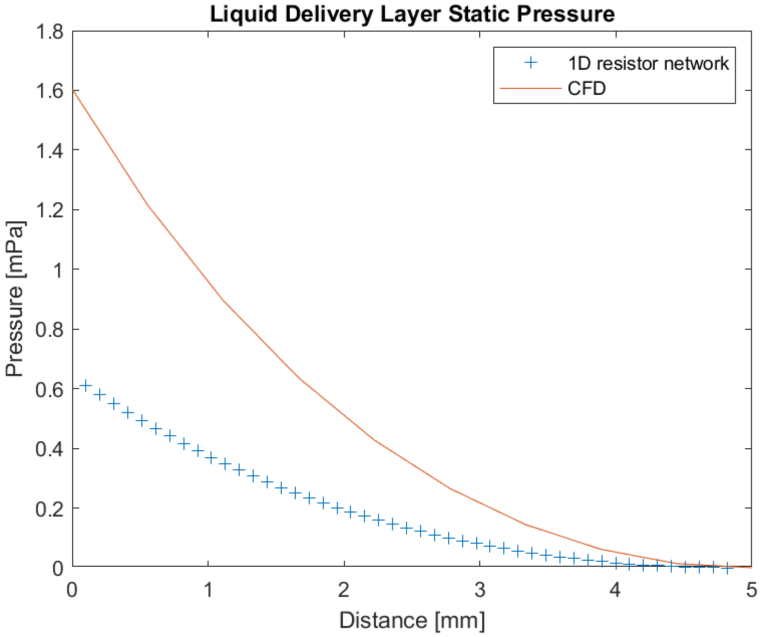

Figure 2.9: Pressure Comparison of 1D Approximation to 2D CFD

The 1D approximation exhibits the same trends as the 2D flow with both solutions showing a non-linear change in static pressure in the LDL. However, it under predicts the overall pressure loss in the system. This is due to the 1D model not accounting for the entrance effects for each pillar, because it assumes that the flow through the entire system is fully developed. It also does not account for the additional losses that would occur in order to turn the flow and have it flow vertically. Despite these assumptions, the resistance model still provides a good approximation of the system, with the maximum difference between the 1D model and the 2D CFD being 37.47%.

The flowrate calculated from the resistor model and CFD is compared in fig. 2.10 below.

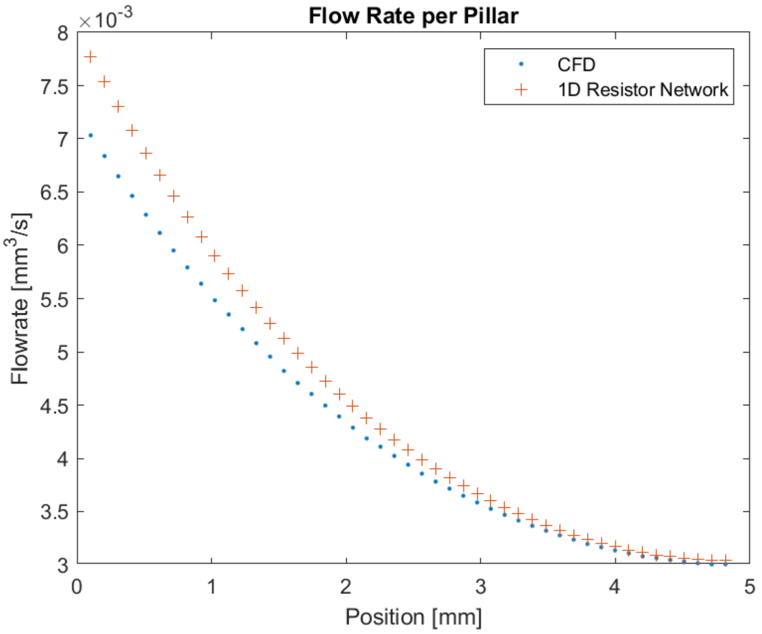

Figure 2.10: Flowrate Comparison of 1D Approximation to 2D CFD

The 1D approximation is more accurate when calculating the flowrate through each pillar, with a maximum difference is 10.53%. This is because both the 1D approximation and the CFD model both conserve mass, so the total flow rate through both systems has to be the same.

Expansion of the Resistance Model

Since the 1D model has been validated against the 2D CFD data, further geometry studies can be rapidly conducted using this model. One such study looks at having a gradient of pillar heights along the array. The resistance to flow is increased by having taller micropillars at the outside of the array. This drives down the flowrate through those pillars, and the overall deviation in flowrate can be minimized as shown in fig. 2.11 below. The flowrate difference is calculated as the difference in flowrate through the current pillar and the last pillar.

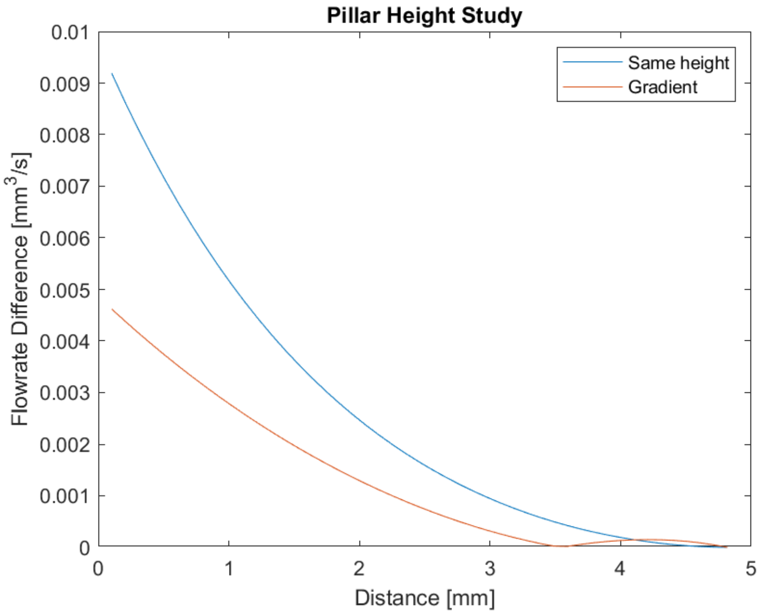

Figure 2.11: Impact of Pillar Height Gradient on Flowrate Difference

This demonstrates one of the possible expansion of the resistance model for rapidly assessing future lateral flow geometries without the need for detailed CFD.

2.5.2 180° Turn Results

Design of Experiments Results

A Design of Experiments (DOE) was conducted on the 180° Turn geometry in order to analyse the interactions and main affects of the different design parameters on the velocity delta across the array.

An interaction plot is used to analyze the results of all 144 trails in the DOE. It allows for a qualitative comparison of each design parameter's impact on the output variable. The Y axis of each plot represents the Velocity delta between the inner and outermost pillars, and each X axis is related to the design parameter in the corresponding column. The interaction plot is shown below in fig. 2.12.

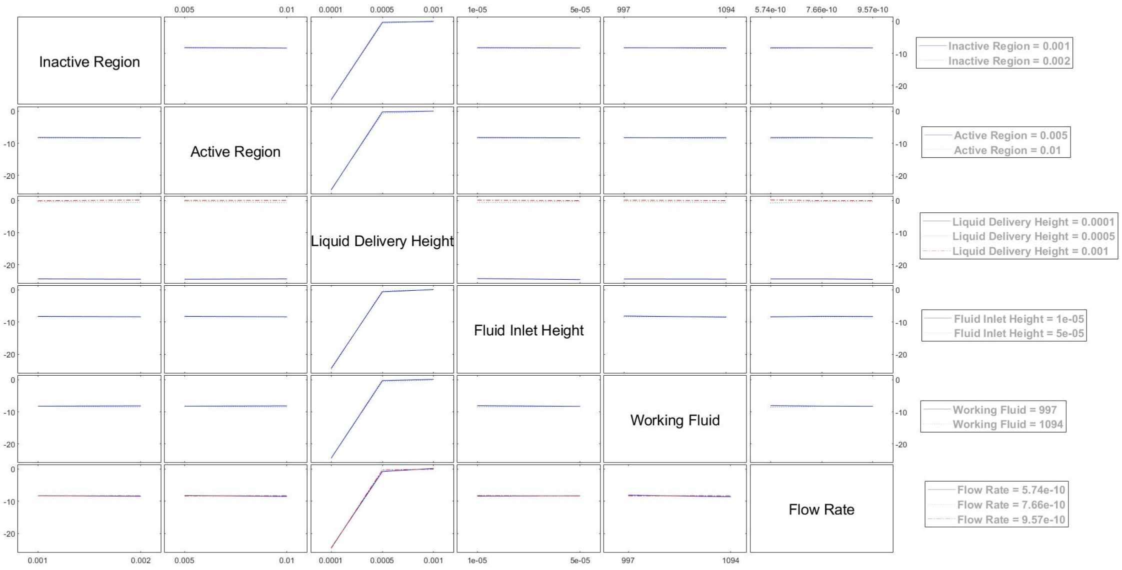

Figure 2.12: Interaction Plot Comparing the Velocity Delta Across All Design Points

The interaction plot demonstrates that for the given bounds under study, only the liquid delivery layer height has an impact on the velocity delta. The inactive region width, active region width, fluid inlet height, working fluid, and flow rate do not impact the velocity delta. This demonstrates that as long as future evaporator designs utilize similar flowrates, working fluids, and active regions, all future efforts can focus only on the LDL height in order to maintain uniformity of the flow through each pillar.

Even though the DOE demonstrated that the 180° turn functions the same as the Lateral Flow geometry,it serves as the launching point for future design work if the geometry significantly increases in size, or if the flowrates through the system drastically increase.

Chapter 3

Prototype Development/Manufacturing

3.1 Proof of Concept

A prototype evaporator was developed in parallel with the analytical and numerical modeling of the liquid delivery layer. Additional constraints were placed on the prototype, in addition to the constraints laid out in manifold development, and are listed below:

1. The manifold needs to able to hold a pressurized working fluid up to 15 Bar
2. The evaporator must have a thermal conduction path to the heat source
3. There needs to be an outlet for any flooding that may occur in the vapor chamber of the evaporator
4. An upper manifold needs to be developed to transition from a single inlet to the square perimeter that is used around the liquid delivery layer
5. In the case of flooding, there must be an area for liquid to be routed out of the vapor chamber

The copper pedestal is bonded to the evaporator to conduct from the heater to the evaporator, and the upper manifold is used to transition the flow from the single inlet fitting to the square perimeter of around the evaporator. Lastly, the liquid bypass is used to remove any of the liquid in the vapor region if the evaporator floods. Figure 3.1 and 3.2 show an exploded view and a section view of the prototype assembly.

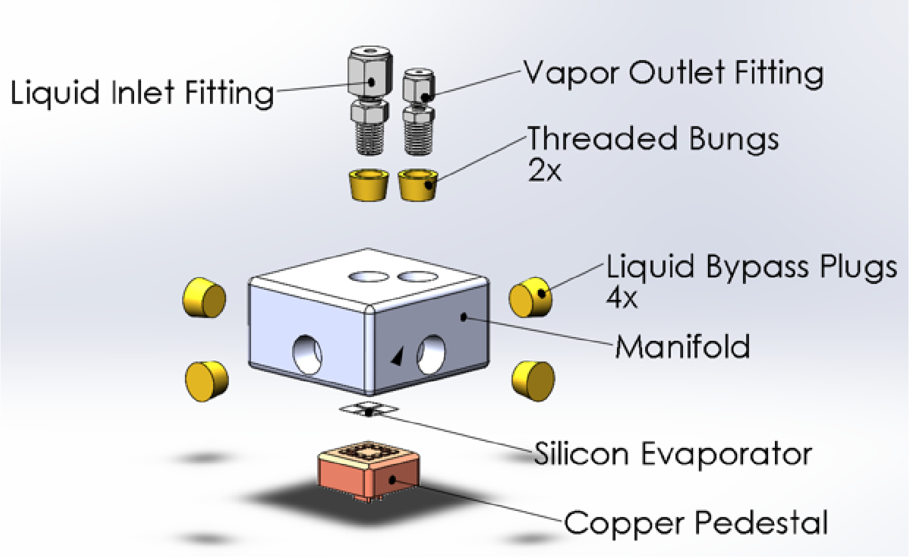

Figure 3.1: Prototype Exploded View

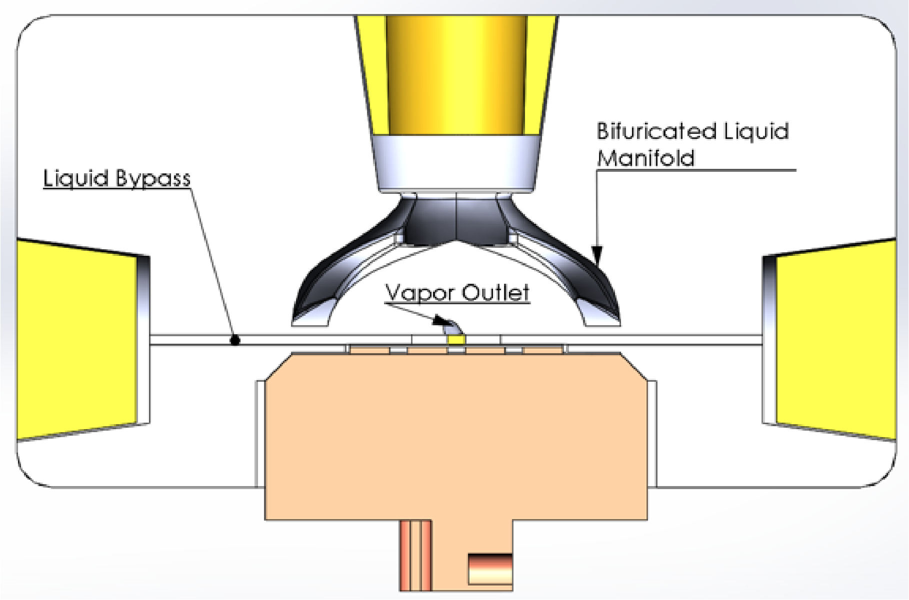

Figure 3.2: Prototype Section View

3.1.1 Material selection

The next step in creating the manifold prototype was to determine the appropriate manufacturing process and materials. The material chosen for the manifold needed to be compatible with the working fluid, R245-fa, in addition to being able to support the thermal and mechanical loads present in the system. Below is a table of candidate materials made with a variety of additive manufacturing processes.

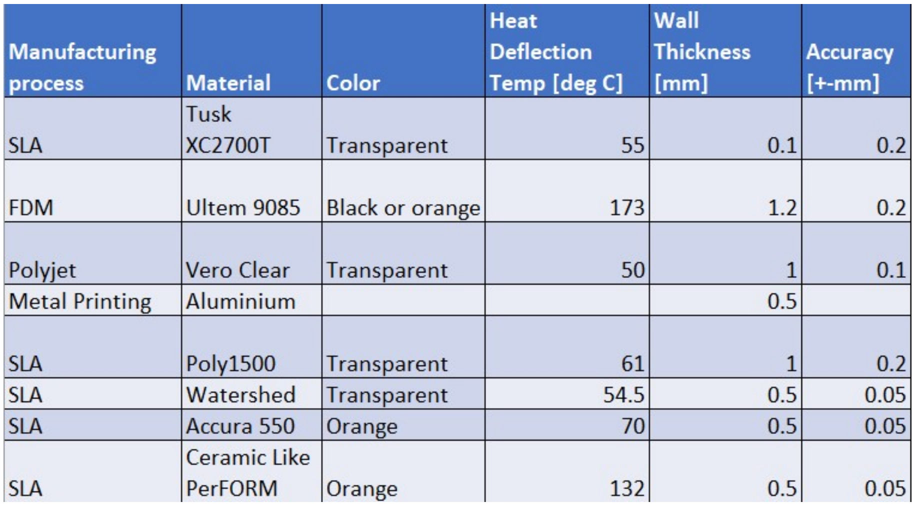

Manufacturing process	Material	Color	Heat Deflection Temp [deg C]	Wall Thickness [mm]	Accuracy [+-mm]
SLA	Tusk XC2700T	Transparent	55	0.1	0.2
FDM	Ultem 9085	Black or orange	173	1.2	0.2
Polyjet	Vero Clear	Transparent	50	1	0.1
Metal Printing	Aluminium			0.5	
SLA	Poly1500	Transparent	61	1	0.2
SLA	Watershed	Transparent	54.5	0.5	0.05
SLA	Accura 550	Orange	70	0.5	0.05
SLA	Ceramic Like PerFORM	Orange	132	0.5	0.05

Figure 3.3: Table of candidate material properties

The working temperature was chosen to be 100° C with a saturation pressure of 10 Bar. This eliminated several potential materials as they had lower heat deflection temperatures than the saturation temperature. Any deflection in the manifold over time due to the internal pressure would lead to leakage and a failure of the device. The Ceramic Like PerFORM was chosen as the desired material, as its heat deflection temperature was greater than the saturation temperature. Additionally, it had a high accuracy and low wall thickness due to the sterolithography printing process, making it ideal for the mating features present in the manifold.

3.1.2 Interfacial materials and epoxies

Two different interfacial material were used to seal and thermally bond the manifold to the evaporator and thermal test vehicle. Several tests were conducted with different surface preperation methods and epoxies. The thermal interface material used is the 8329TCM high thermal conductivity epoxy. [7]

3.2 Physical Prototypes/Testing

3.2.1 Assembly Processes

Before assembly, all mating surfaces(except on the evaporator) were sanded to 200 grit and then cleaned with isopropyl alcohol in order to achieve a good bond. The three images in fig. 3.4 below show the assembly process for the evaporator onto the manifold.

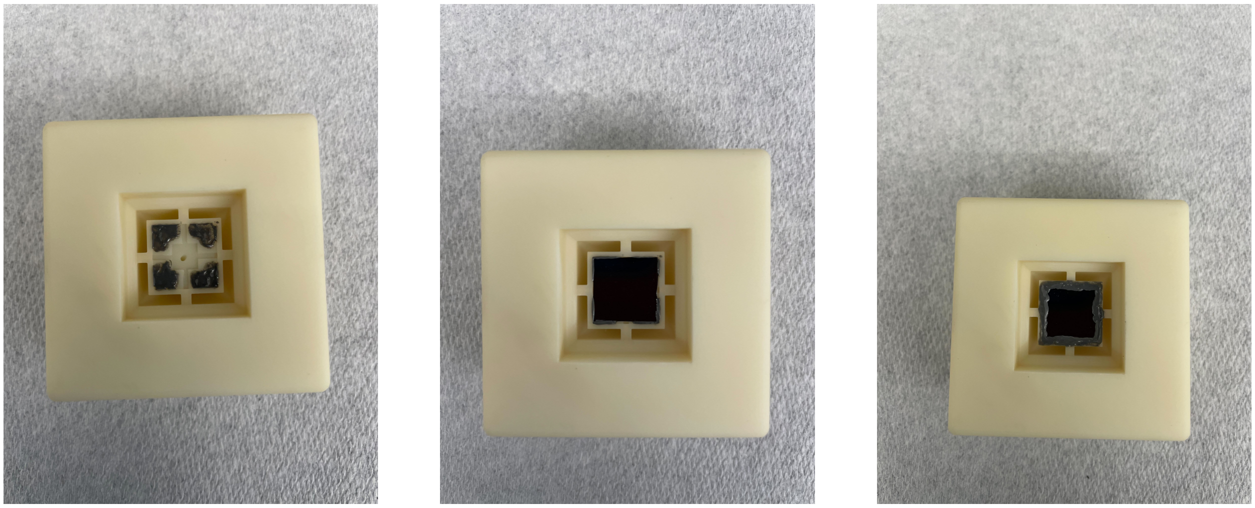
(a) Initial Adhesive (b) Placing The evaporator (c) Sealing the Evaporator

Figure 3.4: Evaporator and Manifold Assembly Steps

Failed Assemblies

The figure below shows an example of an evaporator that failed while testing different surface preparation methods and adhesives.

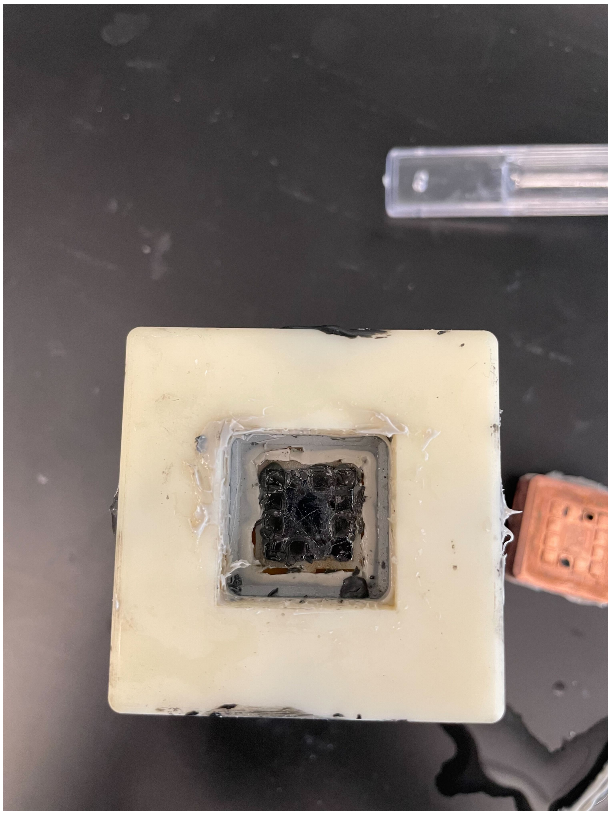

Figure 3.5: Image of a Failed Assembly

This assembly process failed in two ways. The adhesive/sealant failed a pressure test at 6bar, and after disassembly, it can be seen that the sealant also clogged the liquid path from the upper manifold to the evaporator. This demonstrates that not only is the adhesive and surface preparation method critical, but the amount of adhesive applied can have a significant impact on the function of the device.

3.2.2 Experimental Setup

Advanced Cooling Technologies provided the testing facilities, equipment, and measurement devices to test this prototype manifold. A pump was not able to be procured to match the desired flow rate of the system, so instead a thermosyphon was constructed to test the passive performance. A diagram of the thermosyphon, as well as an image of the experimental setup is shown in fig. 3.6 and 3.7.

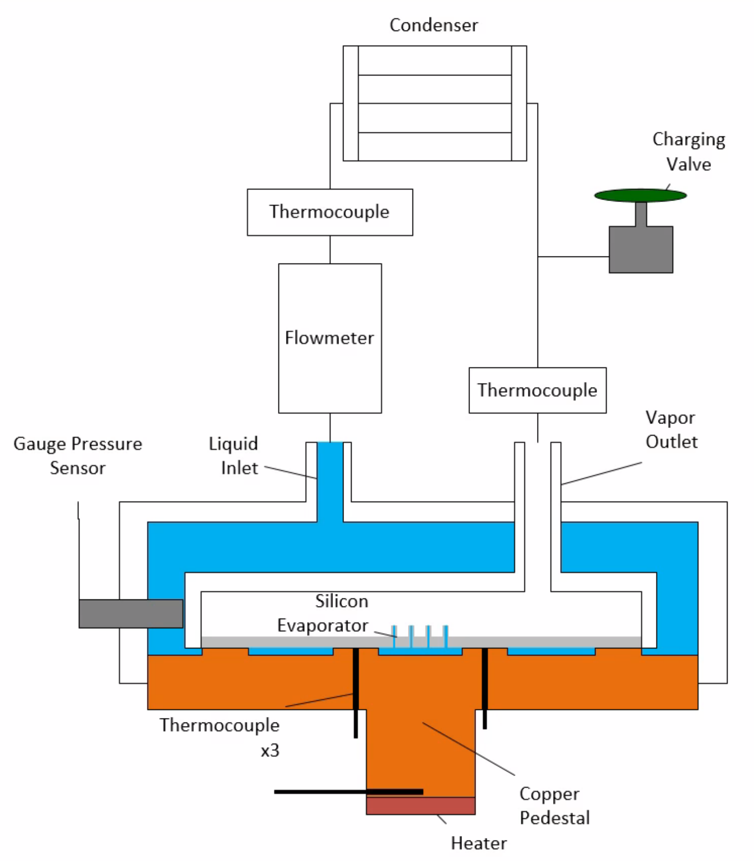

Figure 3.6: Diagram of the Thermosyphon experimental setup

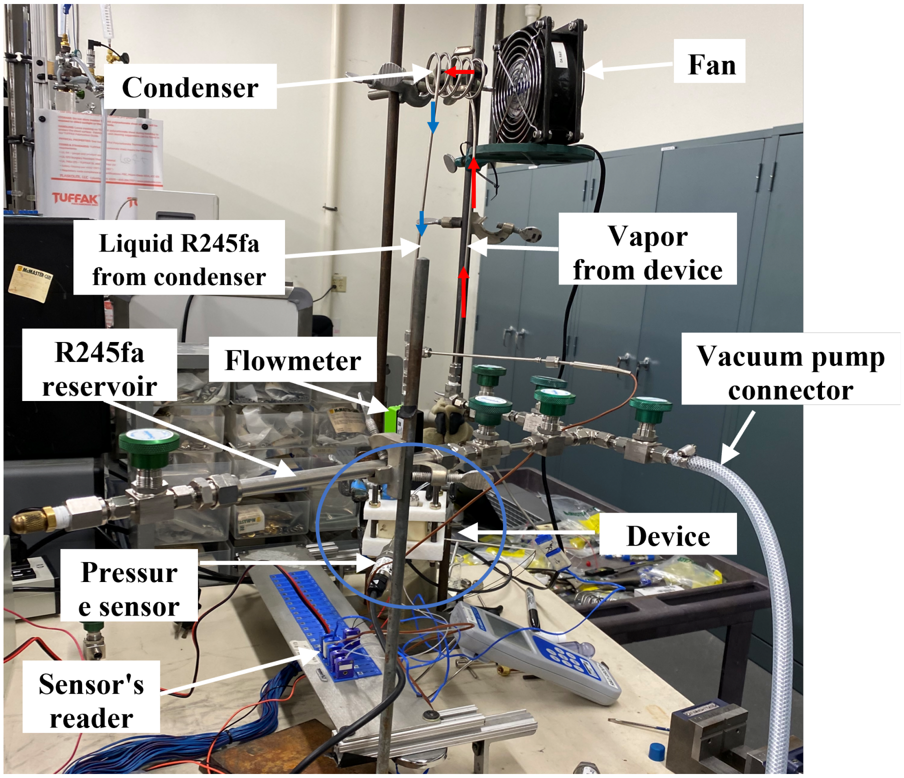

Figure 3.7: Image of the thermosyphon test setup

As noted in the introduction, a thermosyphon is not able to produce pressure heads great enough to achieve the desired droplet shape at this scale, so the testing would not be reflective of the performance of convex microdroplets. Instead the droplet shape would most likely be concave inside the micropillars, however this was not able to be validated, as the droplets were not visible inside the manifold.

3.2.3 Results

The thermosyphon testing demonstrated that the assembly processes enabled conduction between the copper pedestal and the evaporator, did not clog any of the fluid delivery paths, and that the manifold was able to hold a pressurized system of R245-fa for at least a few days with no reduction in internal pressure. Additional results were not able to be obtained due to limited testing time onsite with Advanced Cooling Technologies.

Chapter 4

Conclusion and Future Work

4.1 Conclusion

4.2 Extension into 3D

All simulations and approximations provided in this work are for 2D flow. Since the nature of the flow in the liquid delivery layer is inherently 3D with flow coming in from the perimeter from the evaporator, 3D simulations of specific geometries need to be conducted of the lateral and 180 deg turn geometries in order to validate the results of the 2D models. The boundary conditions developed here can still be applied, so the only work required is to create a parametric 3D model and generate a new mesh to understand the impact of the 3D flow.

4.3 Parametric Models

One of the primary focuses of this research is to develop parametric models that can be quickly adjusted such that when a target heat flux, array size, and die area are identified, the liquid delivery layer can be simulated and a target geometry can be optimized. The sections below details the adjustable parameters, as well as the steps required to successfully simulate a new geometry.

Resistance Model

Several modifications to the evaporator have been proposed, including using a porous membrane under the evaporator to conduct between the chip and evaporator. This additional resistance can be added into the resistance model using the modified Ergun Equation shown below [11].

$$F'_k * \frac{\epsilon^3}{1-\epsilon} = B + \frac{A * (1-\epsilon)}{N'_{Re}} \tag{4.1}$$

where

$$F'_k = \frac{-\nabla P}{\rho V_o^2} D_{eq} \tag{4.2}$$

$$N'_{Re} = \frac{\rho V_o D_{eq}}{\mu} \tag{4.3}$$

and where ϵ is the porosity of the porous medium [unitless], and D_{eq} is the characteristic length of the medium [m], ∇ P is the pressure gradient across the porous medium $[Pa/m]$, and V_o is the superficial velocity $[\frac{m}{s}$ calculated by $V = Q/A$, where Q is the flowrate $[m^3/s]$ and A is the surface area of the porous medium perpendicular to the flow direction $[m^2]$. A and B are experimentally determined parameters used to define the porous medium.

The Ergun Equation can be modified to fit into the resistance formulations provided in Chapter 2, and would allow for the rapid qualitative evaluation of the impact of a porous medium on the hydraulic performance of the evaporator.

4.4 Future Numerical Modeling

4.4.1 Introduction of Heat Transfer

The current CFD models do not account for the change in the flow domain due to buoyancy.Adding heating to the bottom surface of the fluid domain could have ramifications on the development of the velocity profile in the liquid delivery layer, as it would add an additional component of the velocity in the vertical direction. Microposts should also be added to the 3D CFD simulation to capture their impact on the flow in the LDL. The addition of microposts also adds a new region of optimization, as the layout of the microposts will have a significant impact on the flowrate through the micropillars above them. An example evaporator with microposts is shown in fig. 4.1 below

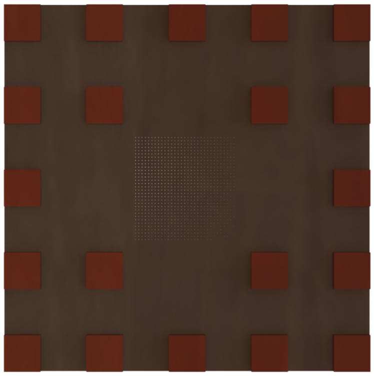

Figure 4.1: Render of the Evaporator Bottom with Copper Microposts

An additional thermal consideration would be to conduct a steady state and transient thermal simulation on the evaporator. This would allow for a better understanding on the actual evaporation rate of each droplet, as it is currently assumed that the entire evaporator is at a uniform temperature. It would also be necessary to capture the temperature gradients present in the evaporator in the presence of non uniform heat fluxes.

4.4.2 Multi-Phase Models

Lastly a transient multi-phase model should be created to model the transient response of the evaporator. Ultimately, the ability to implement a hollow micropillar evaporator relies upon the robust and consistent operation of the device despite variations in heat loads, inlet velocities, and manufacturing tolerances. A multi-phase model would allow for a better understanding of how the hydraulic performance of the evaporator changes as the droplet size changes. Detailed transient models would allow for the formation of a Reduced Order Model which would assist in the creation of a control system to adjust the flowrate to the system depending on other measured variables.

4.5 Manufacturing

Finally, the shape of the evaporator should be adjusted to improve the mating features with the manifold and heat generating element. Lap Joints can be used to increase the adhesive area, and square locating features could be cut to serve as locating features. Additionally the copper structure used to connect the heat generating element to the evaporator should be grow or deposited onto the evaporator to reduce thermal resistance and improve manufacturing and assembly consistency.

References

[1] Ansys fluent, 2020 r2, help system,fluent theory guide, [4.1.1].

[2] Ansys fluent, 2021 r1, help system,fluent theory guide, [1.2.2].

[3] Solomon Adera, Dion S. Antao, Rishi Raj, and Evelyn N. Wang. Hotspot thermal management via thin-film evaporation—part i: Experimental characterization. *IEEE Transactions on Components, Packaging and Manufacturing Technology*, 8(1):88–98, 2018.

[4] Damena D. Agonafer, Hyoungsoon Lee, Pablo A. Vasquez, Yoonjin Won, Ki Wook Jung, Srilakshmi Lingamneni, Binjian Ma, Li Shan, Shuai Shuai, Zichen Du, Tanmoy Maitra, James W. Palko, and Kenneth E. Goodson. Porous micropillar structures for retaining low surface tension liquids. *Journal of Colloid and Interface Science*, 514:316–327, 2018.

[5] Damena D. Agonafer, Ken Lopez, James W. Palko, Yoonjin Won, Juan G. Santiago, and Kenneth E. Goodson. Burst behavior at a capillary tip: Effect of low and high surface tension. *Journal of Colloid and Interface Science*, 455:1–5, 2015.

[6] Theodore L. Bergman. *Fundamentals of heat and mass transfer.* J. Wiley amp; Sons, 7th edition, 2011.

[7] MG Chemicals. 8331s silver conductive epoxy adhesive. November 2021 [Online]. url:https://www.mgchemicals.com/downloads/tds/tds-8331S-2parts.pdf.

[8] Sebastian Eyerer, Peter Eyerer, Markus Eicheldinger, Sebastian Sax, Christoph Wieland, and Hartmut Spliethoff. Material compatibility of orc working fluids with polymers. *Energy Procedia*, 129:137–144, 2017. 4th International Seminar on ORC Power SystemsSeptember 13-15th 2017POLITECNICO DI MILANOBOVISA CAMPUSMILANO, ITALY.

[9] Honeywell. Honeywell genetron 245a orc systems brochure. November 2021 [Online]. url:https://www.honeywell-refrigerants.com/europe/wp-content/uploads/2013/03/honeywell-genetron-245a-orc-systems-brochure1.pdf.

[10] Binjian Ma, Li Shan, Baris Dogruoz, and Damena Agonafer. Evolution of microdroplet morphology confined on asymmetric micropillar structures. *Langmuir*, 35(37):12264–12275, 2019. PMID: 31424229.

[11] I. F. Macdonald, M. S. El-Sayed, K. Mow, and F. A. L. Dullien. Flow through porous media-the ergun equation revisited. *Industrial & Engineering Chemistry Fundamentals*, 18(3):199–208, 1979.

[12] Bruce R. Munson. *Fundamentals of Fluid Mechanics*. Wiley, 7th edition, 2013.

[13] Mun Mun Nahar, Binjian Ma, Kidus Guye, Quan H. Chau, Jorge Padilla, Madhusudan Iyengar, and Damena Agonafer. Review article: Microscale evaporative cooling technologies for high heat flux microelectronics devices: Background and recent advances. *Applied Thermal Engineering*, 194:117109, 2021.

[14] Alisha Piazza, Sougata Hazra, Ki Wook Jung, Michael Degner, Man Prakash Gupta, Edward Jih, Mehdi Asheghi, and Kenneth E. Goodson. Considerations and challenges for large area embedded micro-channels with 3d manifold in high heat flux power electronics applications. In *2020 19th IEEE Intersociety Conference on Thermal and Thermomechanical Phenomena in Electronic Systems (ITherm)*, pages 77–82, 2020.

[15] Yuri O. Popov. Evaporative deposition patterns: Spatial dimensions of the deposit. *Phys. Rev. E*, 71:036313, Mar 2005.

[16] Myung Ki Sung and Issam Mudawar. Single-phase and two-phase hybrid cooling schemes for high-heat-flux thermal management of defense electronics. In *2008 11th Intersociety Conference on Thermal and Thermomechanical Phenomena in Electronic Systems*, pages 121–131, 2008.

[17] Advanced Cooling Technologies. Thermosyphons. March 2021 [Online]. url:https://www.1-act.com/resources/heat-pipe-fundamentals/different-types-of-heat-pipes/thermosyphons/.

[18] Frank M. White and Joseph Majdalani. *Viscous Fluid Flow*. McGraw-Hill, 4th edition, 2022.

[19] Chi Zhang, James W. Palko, Michael T. Barako, Mehdi Asheghi, and Kenneth E. Goodson. Design and optimization of well-ordered microporous copper structure for high heat flux cooling applications. *International Journal of Heat and Mass Transfer*, 173:121241, 2021.

Vita

Alexander Dutton

Degrees	B.S. Mechanical Engineering and Materials Science, December 2021 M.S. Mechanical Engineering and Materials Science, August 2022
Professional Societies	Society of Automotive Engineers Pi Tau Sigma

August 2022